2026 IEEE International Conference on Robotics and Automation (ICRA 2026)
June 1-5, 2026. Vienna, Austria

A Type of Actuator with Large Deformation and Load Capacity: Design and Modeling

Lingzhe Meng, Xinyu Wang, Zhuhong Ying, Mingxuan Ding, Peng Jia, Feihong Yun, Gang Wang*

Abstract—**Flexible actuators have garnered extensive attention due to their flexibility and versatility. However, they still exhibit significant limitations in load capacity and structural stiffness. We have developed a multifunctional rigid-flexible coupled actuator with large deformation and high load capacity. We first investigated the structural design and material selection of the actuator. When establishing the mechanical model, we found that conventional methods could not solve it and that geometric nonlinearity could not be neglected. Therefore, we proposed a rigid-flexible coupled multibody dynamics modeling method suitable for large deformations and conducted static experiments to obtain a nonlinear torque–rotation angle curve. Finally, we compared the simulation results with the dynamic experimental results, demonstrating the effectiveness and accuracy of the proposed method.**

I. Introduction

With the rapid development of robotics, the mobile robot platforms employing different types of actuators have achieved success in many fields, and legged robots represent a current research hotspot [1]. Legged mobile robots exhibit remarkable adaptability and versatility in complex terrains, such as gap environments or unstructured scenarios, showing broad application prospects, particularly in amphibious environments and rugged terrain exploration [2]. Among these, flexible leg structures can effectively absorb energy through deformation, reducing vibration and damage, thereby further enhancing the robot's stability and durability.

Flexible actuators have attracted widespread attention due to their biological-like compliance, safety, and multifunctionality, especially in the design and analysis of actuator flexibility, representing an important development direction in the field of robotics. However, as they are primarily composed of soft materials such as silicone elastomers, significant limitations remain in load-bearing capacity and structural stiffness [3]. In recent years, researchers have attempted to address these issues through new materials, novel manufacturing processes, and structural innovations. For example, ART designed a deformable and adaptive morphology to suit amphibious environments [4]; Wang et al., inspired by biological scales, developed the soft and flexible SAILS structure [5]. Flexible components are prone to wear and fatigue; to further improve durability and load capacity, rigid-flexible coupled designs have gradually become a research focus. Kim and Yamano et al. proposed devices embedding both rigid and flexible elements [6], [7]; Salvietti et al. designed an actuated palm with rigid phalanges and flexible joints [8]; Sun and Low et al. developed grippers combining soft continuous fingers with rigid palms [9], [10]; HERO-BLUE implemented a bionic fin with a passive locking mechanism via silicone and rigid limit structures [11].

Despite these advances, the design and modeling of flexible actuators under large deformations, large rotations, and coupled rigid-body motions remain challenging, especially the nonlinear variation in stiffness exhibited by actuators during large deformations [12]. The modeling, simulation, and experimental methods for rigid-flexible coupled actuators are not yet mature, limiting their application in mobile robot platforms. Addressing these shortcomings could enable flexible robots to enter entirely new application scenarios, potentially equipping them with excellent load-bearing capacity and environmental adaptability on land, or allowing them to swim with agility and flexibility in water (such as sea lions and fish).

A. Design Based on the Front Fin of a Sea Lion

After hundreds of millions of years of evolution, animals have developed forms and modes of motion that are nearly optimal for their environments. Bio-inspiration represents a relevant direction in soft robotics [13]. For example, SpiRobs mimicked the logarithmic spiral patterns of octopus tentacles and elephant trunks to achieve a soft manipulator with flexibility and versatility [14]; Kim et al. used a smart soft composite structure as an actuator to develop a bionic turtle-inspired swimming robot, achieving smooth, soft flapping motions similar to those of a turtle [15]. In these related works, soft actuators were designed for interactive contact with objects or as propulsion devices. We now attempt to address the challenges faced by soft robots in high dynamic impact and heavy load motion operations using a highly adaptable, load-capable, and structurally stiff rigid-flexible coupled actuator. This is similar to the situation encountered by the front flippers of sea lions when moving on land. Their flippers can support them in climbing islands and steep rocky coasts [16]. The front flippers' bones expand in the form of fins, with each phalanx extending into fairly long cartilaginous tips, which together with loose skin and connective tissue form a flexible trailing edge. The front flippers are primarily controlled by muscle groups concentrated in the shoulder joint, analogous to a passive actuator driven by motors. Therefore, we developed a rigid-flexible coupled actuator with passive degrees of freedom. In future research, it may serve as a device for robot propulsion and manipulation.

B. Main Contributions

To address the challenges of insufficient load capacity and dynamic impact resistance in actuators, we propose the Rigid-flexible coupled actuator (RFCA), a multifunctional configuration of a rigid-flexible coupled actuator. It can achieve stable

*This work was supported by the National Natural Science Foundation of China under Grant 52471318.

operation under conditions of heavy loads, large deformations, and high dynamic impacts. Furthermore, it offers versatility and scalability, allowing for adaptive adjustments based on practical requirements. Taking into account geometric nonlinearity under large deformation conditions, we propose a rigid-flexible coupled multibody dynamics model applicable to all similar configurations. By investigating geometric nonlinear effects, we derive a nonlinear equivalent stiffness, enabling the model to accurately solve the actuator's state under various working conditions without adjusting the equivalent stiffness.

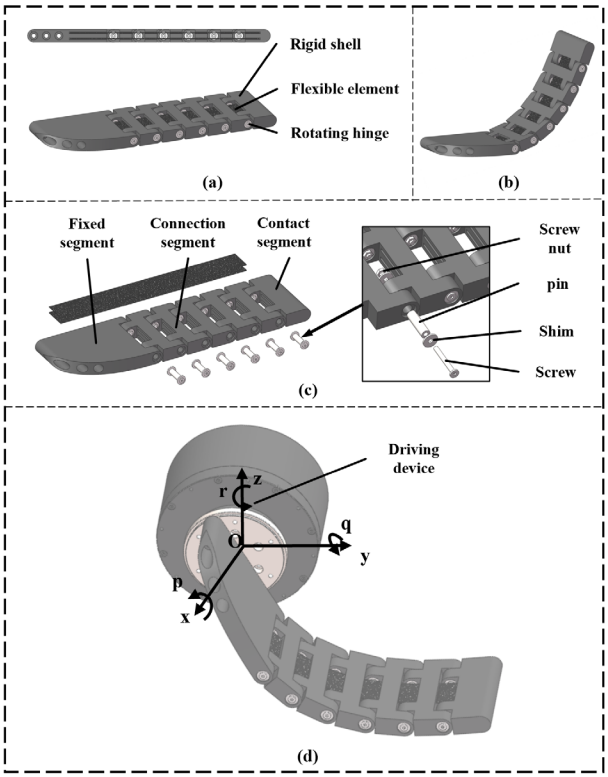

Fig. 1. Model of the RFCA. (a) Overall structure (b) Schematic diagram of force-induced bending (c) Fabrication process diagram (d) Usage schematic diagram.

II. Design and Structure

A. Structure

Figure 1 (a) shows the composition of the RFCA, which mainly consists of hinges, a rigid shell, and flexible elements. Coupling the rigid shell with the flexible component not only protects the fragile flexible components from external wear and stress concentration damage, but also provides excellent load-bearing capacity, stability, and flexibility.Its overall dimensions and detailed shape are not fixed and can be adaptively adjusted according to practical application scenarios without changing the underlying mechanism principle. We fabricated a prototype using the sea lion's front flippers as a reference for size and performance. Its length is 290 mm, its width is 80 mm, its thickness is 15 mm, and it weighs only 0.32 kg. As shown in Figure 1 (b), it can undergo continuous flexible deformation under external forces.

Figure 1 (c) illustrates the detailed structure and assembly process of each component. Among these, the hinge shaft is composed of screws, washers, cylindrical pins, and nuts made of 304 stainless steel. The rigid shell is manufactured using PA12 nylon via powder sintering technology, offering high structural strength, light weight, and resistance to extreme environments. The overall structure of the rigid shell consists of multiple segments with different functions, categorized into fixed segments, connection segments, and contact segments. Each segment is equipped with mounting bases adapted to the hinge shaft, which form hinges when combined with the shaft to connect the segments. The mounting bases are designed with appropriate grooves to conceal protruding parts of the shaft, improving efficiency during underwater use. As shown in Figure 1 (d), key capabilities such as rotation and contact are achieved by connecting the fixed segment to the driving device. The segment and hinge connection mechanism endows the actuator with a large number of passive degrees of freedom, significantly enhancing its flexibility and compliance. The number and positions of contact segments and connection segments are not fixed in the structure. Connection segments serve to link and extend the structure. The parts that need to interact and collide with the external environment during operation are contact segments, which can be made of special contact materials or equipped with suitable friction structures to better achieve target functions.

We fabricated a special carbon fiber spring piece (CFSP) as the flexible element. It is made of epoxy resin and carbon fiber cloth through high-temperature baking and extrusion molding, and its physical properties differ significantly from those of carbon fiber boards made from woven carbon fiber fabric. In our RFCA, the CFSP is 226 mm long, 25.4 mm wide, and only 0.8 mm thick. In practical applications, its flexibility and strength can be adjusted by changing its physical dimensions. For example, an RFCA equipped with a 0.3 mm-thick spring piece exhibits physical properties similar to a fish's tail. As shown in Figure 1 (a), two spring pieces are symmetrically embedded into the assembled rigid shell, effectively reducing stress concentration and adding redundant safety. During assembly, the flexible elements and the rigid shell form a complex rigid-flexible coupled structure. It exhibits continuous flexible deformation characteristics but is constrained by limited passive degrees of freedom, making it difficult to model and solve as either a pure rigid-body system or a flexible body.

Compared to the Propeller-Leg of SHOALBOT [17], the RFCA offers better bio-inspired approximation, giving it advantages in reducing entanglement risks and environmental disturbances. Compared to the pectoral fin of HERO-BLUE [11], this design is simpler and more compact, with stronger load-bearing capacity. Compared to the Transformable Flipper Legs of AmphiHex [18], which achieve multifunctionality through actuated deformation, the multifunctionality of this rigid-flexible coupled structure is inherent.

Fig. 2. Carbon fiber spring piece (CFSP).

B. Selection of Flexible Materials

With continuous breakthroughs in materials and manufacturing technologies, synthetic materials such as silicone rubber (VMQ) and nylon (PA), as well as composite materials like

carbon fiber reinforced polymer (CFRP), are increasingly widely used in the field of robotics. This is owing to their unique advantages over metals, such as the extremely high specific strength of CFRP and the large elastic deformation capabilities of VMQ.

The choice of material for flexible elements directly affects the physical performance of the actuator. To intuitively compare material properties, we conducted a comparative study based on a rectangular material measuring 226 mm × 25.4 mm × 0.8 mm. Table 1 shows the performance parameters of three commonly used materials and the CFSP. The densities of all four materials are relatively low, which helps reduce rotational inertia and improve efficiency. The density of CFSP is similar to that of CFRP, owing to their shared raw materials. VMQ is very soft, while it exhibits excellent bending toughness and deformation capability, its extremely low specific modulus and bending strength result in poor load-bearing capacity, and its ductility makes it difficult to control under high stress and strain. PA12 nylon is a material with strong overall performance, offering excellent stability, suitable hardness and strength, as well as certain toughness and deformation ability, making it highly suitable for use as a rigid shell that absorbs dynamic impacts. CFRP is world-renowned for its extremely high strength and modulus, and its excellent fatigue resistance and corrosion resistance make it the preferred choice for lightweight design. However, the composite structure of woven carbon fiber results in very limited bending toughness and deformation capability, making it unsuitable as a flexible element.

As shown in Figure 2, unlike CFRP, CFSP is manufactured using an extrusion molding process, with its fiber direction aligned with the Y-axis. Along the fiber direction, it not only demonstrates strength and modulus comparable to CFRP but also possesses bending toughness and deformation capability similar to VMQ. Additionally, it exhibits excellent fatigue resistance. When subjected to continuous large-deformation bending fatigue tests at 110° using an Instron ESM303 dynamic fatigue testing machine, it underwent normal deformation for over 10^6 cycles at a target strain of. Therefore, CFSP along the fiber direction is highly suitable as a flexible element for handling large deformations and heavy loads. Moreover, the coupled PA12 shell helps it resist wear and impact, significantly extending the actuator's service life.

TABLE I. PERFORMANCE COMPARISON OF MATERIALS

Para-meter	Unit	Material Name			
		VMQ	PA12	CFRP	CFSP
Density	g/cm³	0.98	1.13	1.60	1.55
Young's modulus	GPa	0.006	2.75	125.46	120
Specific Modulus	GPa/(g/cm³)	0.00061	2.43	78.41	77.42
Poisson's ratio	/	0.47	0.38	0.31	0.28
Bending strength	MPa	9	67	860	651
Flexural toughness	/	Excellent	Average	poor	good
Bending deformation	/	Excellent	Average	poor	good

a. VMQ, PA12, and CFRP are estimated values for common materials.

b. Their dimensions are all 226mm×25.4mm×0.8mm.

III. MECHANICAL MODEL

The RFCA is a special type of rigid-flexible coupled structure. Unlike typical coupled configurations, where a flexible body is connected to a rigid main body, its flexible element is encapsulated within a rigid shell, forming a nested relationship between the two. As a result, it cannot be accurately solved using conventional rigid-flexible coupled mechanical methods or flexible body mechanics approaches. Furthermore, the equivalent stiffness during bending is often treated as a constant, which is valid under small deflections. However, for objects undergoing large deformations with significant deflection, the variation in equivalent stiffness cannot be neglected. To address these gaps, this chapter describes and analyzes the changes in equivalent stiffness for large-deformation objects and proposes static and dynamic solving methods specifically for the RFCA structure. This research holds significant importance for its further application and precise control.

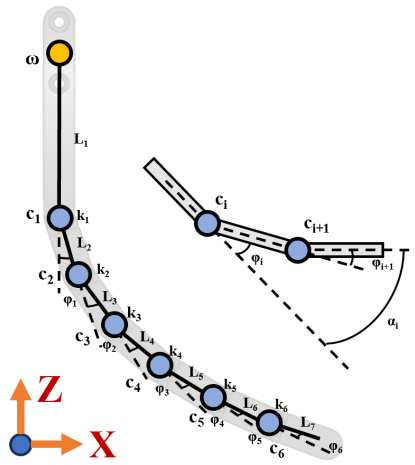

Fig. 3. Parameter definition for mechanical modeling.

A. Equivalent Stiffness Based On Pseudo-rigid-body Model

The concept of the pseudo-rigid body model involves equivalently representing a flexible body as a structure composed of multiple rigid links and hinges to simplify the computation of flexible bodies [19]. This inspires modeling the RFCA structure. The rigid shell of the RFCA is inherently composed of multiple rigid segments connected by hinges. This rigid shell constrains the flexible body to bend only at the hinge locations, thereby providing a natural foundation for a pseudo-rigid-body model of the internally coupled flexible body. Therefore, when equivalently modeling the flexible element of the RFCA as a pseudo-rigid-body model, we align the positions of its virtual hinges with those of the hinges on the external rigid shell (using the 7R model as an example). Based on this alignment, the flexible element is equivalently represented as torsional springs acting at the hinge locations of the rigid shell. This approach not only enables us to rapidly and accurately determine the fundamental parameters of the pseudo-rigid-body model of the flexible body but also resolves the coupled modeling problem between the flexible body and the rigid shell in the RFCA. This modeling method yields favorable results for flexible materials that exhibit stable physical properties and low extensibility.

It is worth noting that the finite element analysis (FEA) method is also commonly used to solve flexible body deformation problems. However, it exhibits poor accuracy, smoothness, and computational efficiency when addressing complex rigid-flexible coupling problems and large deformation scenarios such as those encountered in RFCA.

The equivalent stiffness of these torsional springs exhibits nonlinearity during large deformations. In cantilever beams undergoing large deformations, a geometric nonlinearity phenomenon can be observed where the beam's stiffness increases with deflection. This is primarily caused by changes in curvature:

$$\kappa = \frac{|y''|}{(1+y'^2)^{\frac{3}{2}}} \tag{1}$$

Where $y' = \tan\theta$, when θ is small, $\kappa \approx |y''|$ can be assumed. However, when $\theta \geq 0.27\text{rad}$, the error of this simplified formula exceeds 10%, indicating that geometric nonlinearity cannot be neglected during large deformations. Furthermore, when analyzing the flexible element, since it weighs only 7g, only the bending potential energy is considered in calculating the total potential energy of the system.

$$U = \int_0^L \frac{1}{2} EI\kappa(s)^2 ds \tag{2}$$

$$U_r = \sum_{i=1}^{6} \frac{1}{2} K_i \phi_i^2 \tag{3}$$

$$\delta[U + \sum_{i=1}^{7} \lambda_i(\theta(s_i) - \beta_i)] = 0 \tag{4}$$

Equation (2) represents the bending potential energy of the flexible element, Equation (3) represents the bending potential energy of the equivalent torsional spring, and Equation (4) represents the constraint condition after introducing the Lagrange multiplier. After expanding the calculation, the variational equation of the hinge rotation angle is obtained:

$$\frac{\partial^2 U}{\partial \phi_i^2} = \lim_{\delta\phi_i \to 0} \frac{1}{(\partial\phi_i)^2}[U(\phi_i + \delta\phi_i) - 2U(\phi_i) + U(\phi_i - \delta\phi_i)] \tag{5}$$

The numerical solution is obtained using the Newton-Raphson iteration method and the perturbation method, where the equivalent stiffness K_i is the second derivative of the potential energy with respect to the rotation angle, and the discrete potential energy U is given by Equation (7).

$$K_i = \left.\frac{\partial^2 U}{\partial \phi^2}\right|_{\{\phi_j\}} \tag{6}$$

$$U = \sum_{e=1}^{N} \frac{1}{2}\left(\frac{EI}{\Delta s}\right)(\theta_{e+1} - \theta_e)^2 \tag{7}$$

The final solution for the equivalent stiffness is:

$$K_i = \frac{U(\phi_i + \delta\phi) - 2U(0) + U(\phi_i - \delta\phi)}{(\delta\phi)^2} \tag{8}$$

B. Static Model

When the RFCA structure is applied to static usage scenarios such as grasping or holding, a highly accurate rigid-flexible coupled statics model is of significant importance. The statics model is solved based on the 7R pseudo-rigid body model:

$$\begin{cases} \varphi_k = \sum_{i=1}^{k} \phi_i(t), k = 1,2,\ldots,7 \\ x(t) = \sum_{i=1}^{7} L_i \cos\varphi_i \\ y(t) = \sum_{i=1}^{7} L_i \sin\varphi_i \\ J_{1,\,n} = \dfrac{\partial x(t)}{\partial \phi_n}, n = 1,2,\ldots,7 \\ J_{2,\,n} = \dfrac{\partial y(t)}{\partial \phi_n}, n = 1,2,\ldots,7 \end{cases} \tag{9}$$

Under static conditions, force equilibrium is maintained at the end effector, allowing moment equilibrium equations to be formulated for each node. Finally, the least-squares solution is obtained using the Singular Value Decomposition (SVD) method.

$$\begin{bmatrix} -\sum_{i=1}^{7} L_i \sin\alpha_i & \cdots & -\sum_{i=7}^{7} L_i \sin\alpha_i \\ \sum_{i=1}^{7} L_i \cos\alpha_i & \cdots & \sum_{i=7}^{7} L_i \cos\alpha_i \end{bmatrix} \begin{bmatrix} F_x \\ F_y \end{bmatrix} = \begin{bmatrix} k_1\phi_1 \\ \vdots \\ k_7\phi_7 \end{bmatrix} \tag{10}$$

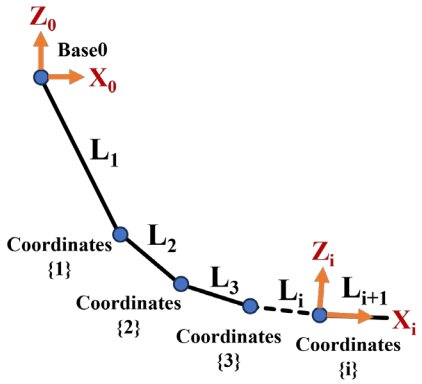

Fig. 4. Establishing coordinate systems using the modified Denavit-Hartenberg parameters method.

C. Multibody System Dynamics Model

As shown in Figure 4, the modified D-H parameter method is adopted to establish coordinate systems for each rigid body. Starting from the base, the coordinate system $\{i\}$ is sequentially assigned to each link i. The Newton-Euler method is used to recursively derive the dynamic equations, and the motion information of the links is calculated through an extrapolation process from the base to the end effector (Equation (11)). Here, α_i represents the absolute angle, ${}^{i-1}R_i$ denotes the rotation matrix, ${}^{i}f_i$ signifies the force exerted by link on link, and ${}^{i}\omega_i$ indicates the relative angular velocity.

$$\begin{cases} \alpha_i = \alpha_1 + \sum_{k=1}^{i-1} \phi_k \quad (i = 2,3,...,7) \\ \hat{Z}_i = \begin{bmatrix} 0 & 0 & 1 \end{bmatrix}^T \\ {}^i\omega_i = {}^{i-1}R_i^T \cdot {}^{i-1}\omega_{i-1} + \dot{\phi}_i \cdot \hat{Z}_i \\ {}^i\omega_i = {}^{i-1}R_i^T \cdot {}^{i-1}\dot{\omega}_{i-1} + {}^{i-1}R_i^T \cdot {}^{i-1}\omega_{i-1} \times (\dot{\phi}_i \cdot \hat{Z}_i) + \ddot{\phi}_i \cdot \hat{Z}_i \\ {}^iP_{ci} = \begin{bmatrix} \frac{a_i}{2} & 0 & 0 \end{bmatrix} \\ {}^iv_i = {}^{i-1}R_i^T ({}^{i-1}\dot{v}_{i-1} + {}^{i-1}\dot{\omega}_{i-1} \times {}^{i-1}P_i + {}^{i-1}\omega_{i-1} \times ({}^{i-1}\omega_{i-1} \times P_i)) \\ {}^i\dot{v}_{ci} = {}^i\dot{v}_i + {}^i\dot{\omega}_i \times {}^iP_{ci} + {}^i\omega_i \times ({}^i\omega_i \times {}^iP_{ci}) \end{cases} \tag{11}$$

Thereafter, the force information of the links is calculated through an introspection process from the end effector to the base (Equation (12)). Here, denotes the moment exerted by link on link, and represents the torque between hinges.

$$\begin{cases} {}^iF_i = m_i \cdot {}^i\dot{v}_{ci} \\ {}^iN_i = {}^iI_i \cdot {}^i\dot{\omega}_i + {}^i\omega_i \times ({}^iI_i \cdot {}^i\omega_i) \\ {}^if_i = {}^{i+1}R_i \cdot {}^{i+1}f_{i+1} + {}^iF_i \\ {}^in_i = {}^iN_i + {}^{i+1}R_i \cdot {}^{i+1}n_{i+1} + {}^iP_{ci} \times {}^iF_i + {}^iP_{i+1} \times ({}^{i+1}R_i \cdot {}^{i+1}f_{i+1}) \\ {}^iP_{i+1} = \begin{bmatrix} a_i & 0 & 0 \end{bmatrix}^T \\ \tau_{n,i} = {}^in_i \cdot \hat{Z}_i - K_i(\phi_i - \phi_{i0}) \end{cases} \tag{12}$$

Following this, the end boundary conditions of the dynamics model are established according to the actual working conditions. The final results can be expressed in matrix form:

$$A(\phi, \dot{\phi}) \cdot z = b(\phi, \dot{\phi}, \tau) \tag{13}$$

D. Dynamic Response

If the rotating shaft rotates at an angular velocity ω, this can be regarded as a kinematic constraint. According to the principle of virtual work, the generalized forces required to maintain this motion will perform work, and its virtual work is $\tau_{motor}\delta\theta_1$, The corresponding term in τ_{ext} is solved by solving a constrained dynamic equation $\dot{\theta}_1 = \omega$. Let the end contact constraint condition be:

$$\begin{cases} y_p(q) = 0 \\ \frac{\partial y_p}{\partial q} \cdot \dot{q} = J_y(q)\dot{q} = 0 \\ J_y(q)\ddot{q} + \dot{J}_y(q,\dot{q})\dot{q} = 0 \end{cases} \tag{14}$$

The dynamic equation for contact with the ground is:

$$\begin{bmatrix} M(q) & J_y^T(q) \\ J_y(q) & 0 \end{bmatrix} \begin{bmatrix} \ddot{q} \\ \lambda \end{bmatrix} = \begin{bmatrix} F(q,\dot{q},t) \\ -J_y(q,\dot{q})\dot{q} \end{bmatrix} \tag{15}$$

For the dynamic equations of a tree-structured multibody system composed of n rigid bodies, Z and z represent the generalized mass matrix and generalized force matrix of the system, respectively. The generalized coordinate matrix $q = (q_1^T \cdots q_N^T)^T$ has a dimension of n. Assuming the kinematic control law of the k-th variable is known, the corresponding generalized variable is q_k, and u_k is the driving force to be solved. Let the driving force matrix be $u = (0 \quad \cdots \quad u_k \quad \cdots \quad 0)^T$. By applying an equivalent transformation to the mass matrix, driving force matrix, and generalized coordinate array, an equivalent formulation that simultaneously computes the forward and inverse dynamics problems of the system can be derived:

$$\begin{bmatrix} Z_{11} & \cdots & 0 & \cdots & Z_{1n} \\ \vdots & & \vdots & & \vdots \\ Z_{k1} & & -1 & & Z_{kn} \\ \vdots & & \vdots & & \vdots \\ Z_{n1} & \cdots & 0 & \cdots & Z_{nn} \end{bmatrix} \begin{bmatrix} \ddot{q}_1 \\ \vdots \\ u_k \\ \vdots \\ \ddot{q}_n \end{bmatrix} = \begin{bmatrix} z_1 \\ \vdots \\ z_k \\ \vdots \\ z_n \end{bmatrix} - \begin{bmatrix} Z_{1k} \\ \vdots \\ Z_{kk} \\ \vdots \\ Z_{nk} \end{bmatrix} \ddot{q}_k \tag{16}$$

E. Contact Model

Coulomb friction is a contact force that impedes the relative motion of objects. Its magnitude is proportional to the positive pressure, and its direction is opposite to the motion trend. It is the main cause of energy consumption and heat generation.

Contact behavior is a ubiquitous issue in mechanical systems. In many cases, constraints and force transmission within mechanical systems are actually achieved through contact. Therefore, essentially, contact can be regarded as a dynamically varying constraint. Assuming the curvature radii of two contacting bodies are R_1 and R_2, and their Young's moduli are E_1 and E_2, where r is the radial distance from the contact center, and δ is the maximum deformation in the contact area, the pressure distribution formula during contact is:

$$\begin{cases} p(r) = \frac{3}{2}E'\left(\frac{\delta}{a}\right)^{\frac{3}{2}}\left(1 - \frac{r^2}{a^2}\right)^{\frac{1}{2}} \\ \frac{1}{E'} = \frac{1-\upsilon_1^2}{E_1} + \frac{1-\upsilon_2^2}{E_2} \\ a = 2\sqrt{\frac{R_1R_2}{R_1+R_2}\delta} \end{cases} \tag{17}$$

Coulomb friction states that once an object begins to move, the frictional resistance acting opposite to the direction of motion can be expressed as a function of the sliding velocity. The resistance f_c caused by Coulomb friction has a constant magnitude, where μ_k is the kinetic friction coefficient and f_n is the normal force, which can be expressed as:

$$\begin{cases} f(v) = f_c \operatorname{sgn}(v) \\ f_c = \mu_k |f_n| \end{cases} \tag{18}$$

Let f_s be the maximum static friction force. When $\nu = 0$, the friction force is a function of the external force. When $\nu \neq 0$, the friction force can be expressed in the form of Coulomb friction:

$$f = \begin{cases} f_e, & v = 0,\ |f_e| < f_s \\ f_s \operatorname{sgn}(f_e), & v = 0,\ |f_e| \geq f_s \\ f_c \operatorname{sgn}(v), & v \neq 0 \end{cases} \tag{19}$$

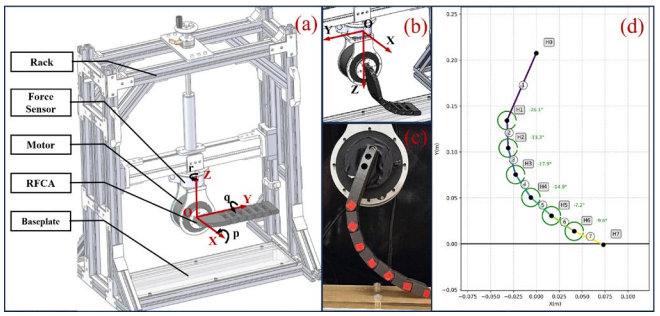

Fig. 5. Experimental setup and methods. (a) Experimental setup and rotational shaft coordinate system (b) Force sensor coordinate system (c) Photograph of the flapping experiment (d) Static model diagram obtained from visual data.

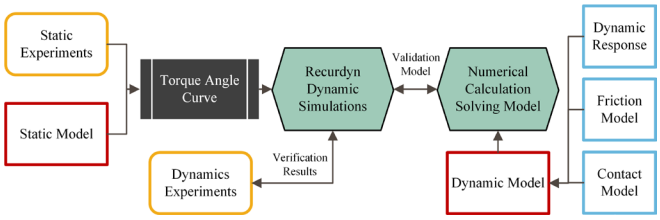

Fig. 6. Simulation flowchart.

IV. Experiments and Results

A. Experiments

As shown in Figure 6 (a), the experimental setup consists of an overall frame constructed from aluminum alloy profiles, with height adjustment and limitation achieved through lead screws and guide rails. Its base plate is a flat acrylic board used to simulate the ground. It is equipped with an ATI Gamma model 6-axis force sensor with a sampling frequency of 15,000 Hz, capable of measuring forces and moments along the three axes as illustrated in Figure 6 (b). The motor is fixedly connected to it to approximately measure the force conditions at the rotating shaft. The RFCA is mounted on the motor's rotating shaft, which provides the rotational driving force. During experiments, limited by the frame height, the RFCA contacts the simulated ground during rotation, resulting in deformation and friction. This process is similar to the locomotion mechanism of legged mobile platforms. Studying and solving the statics and dynamics of this motion process can provide important theoretical and practical foundations for further applications of the RFCA.

We first conducted dynamic impact performance tests to verify its load capacity and impact resistance. The motor shaft was fixed at a height of 155 mm from the contact surface, and the RFCA was driven at a rotational speed of 15 rad/s while continuously colliding with the contact surface. Under test conditions, it could withstand deformation forces and impact loads of approximately 300 N multiple times without damage. Taking the peak test point as an example, the force along the sensor's Z-axis was 232 N, and the force along the Y-axis was 188 N. This means it can provide a driving force of 188 N under a load of 23.7 kg. In addition, the trial-produced RFCA sample demonstrated good deformability in the bending test. Under forced bending conditions, the angle between the contact segment and the fixed segment was not less than 130 degrees, which is beneficial for absorbing high-dynamic impacts.

The torque-rotation angle curve of the hinge is the core data we need to obtain experimentally. Its first derivative represents the value of equivalent stiffness at the corresponding rotation angle, and it is an inherent property influenced only by structure and material. Based on this characteristic, it can be acquired and calculated through static experiments, significantly reducing costs compared to the stringent hardware requirements of dynamic experiments. Therefore, the experiment consists of two parts: static experiments and dynamic experiments, aimed at obtaining the torque-rotation angle curve and verifying the accuracy of the dynamic model, respectively. The specific workflow is shown in Figure 6. In the static experiment section, as shown in Figure 5 (c), the background is set to pure black, and each hinge and the end are marked in red. These measures effectively ensure the accuracy of visual recognition of hinge rotation angles. The experiment incrementally increases the rotation angle of the shaft in stages at the same frame height, acquiring state parameters from the force sensor and motor after stabilization and capturing high-definition photos for visual processing. In the dynamic experiment section, the RFCA undergoes flapping motions at different driving speeds and frame heights. High-frequency state parameters, primarily the angular velocity of the shaft and the force along the Z-axis, are obtained from the force sensor and motor. Furthermore, as the contact area and position between the RFCA and the ground continuously undergo significant changes during rotation, the contact force with the ground is difficult to measure precisely. Although we measure the shaft force as a substitute, this results in computational results from the model that cannot be directly compared with experimental results. To address this issue, we import identical settings as the theoretical model into the RecurDyn simulation software to simultaneously solve for both contact force and shaft force.

TABLE II. Experimental Results

Rack Height	Speed (rad/s)	Experimental Valley Value	Simulated Valley Value	Error(%)	
215mm	2.433	(1.10,-54.97)	(1.05,-53.32)	4.5	3.0
215mm	3.249	(0.80,-52.41)	(0.78,-51.54)	2.5	1.7
235mm	2.478	(0.97,-41.18)	(0.97,-42.34)	0.0	2.8
235mm	3.276	(0.69,-39.19)	(0.73,-40.46)	5.8	3.2

a. The above experimental data represent the average value of five sets of data for each condition.

B. Simulations and Results

To accurately implement the proposed rigid-flexible coupled dynamics model into the RecurDyn simulation software, we developed a program based on the theoretical model and solution methodology described above, incorporating identical simulation parameters. This implementation yielded a simulated contact force curve for the RFCA during ground flapping. Subsequently, we configured an equivalent model in RecurDyn with precisely the same parameters and boundary conditions to perform a parallel simulation. As shown in Figure 7 (a), the two resulting curves exhibit excellent agreement

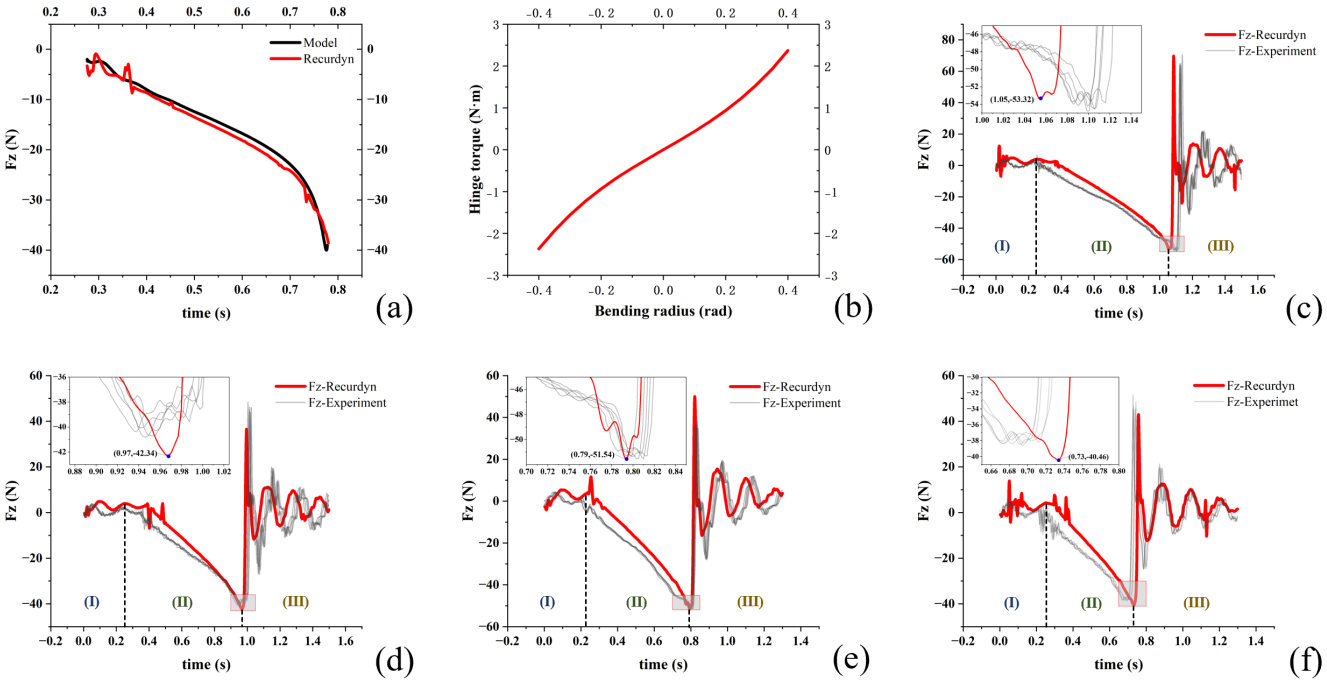

Fig. 7. Experimental and simulation results. (a) Comparison between theoretical model calculations and Recurdyn simulation results (b) Torque–rotation angle curve (c) Five experimental and simulation results under frame height 215 mm and average rotational speed 2.433 rad/s (d) Five experimental and simulation results under frame height 235 mm and average rotational speed 2.478 rad/s (e) Five experimental and simulation results under frame height 215 mm and average rotational speed 3.249 rad/s (f) Five experimental and simulation results under frame height 235 mm and average rotational speed 3.276 rad/s.

in trend, with a relative error of 4.91%. This close correspondence validates that the RecurDyn simulation setup is consistent with our analytical model.

Following this, we conducted dynamic simulations in RecurDyn using parameters consistent with the experimental conditions to compute the force state at the rotating shaft of the mechanism. The torque–rotation angle curve (Figure 7 (b)), obtained through static experiments and theoretical derivation, exhibits significant nonlinearity, with the equivalent stiffness increasing as the rotation angle grows. Furthermore, the motor speed under dynamic loading conditions is unstable. We used the average motor speed as a simulation parameter to reduce computational complexity, but this causes the simulation results to show minor phase advances or lags compared to the actual data. As shown in Figure 7 (c–f), the simulation results slightly lag behind the experimental data in regions (I) and (II) and slightly lead in region (III). Nevertheless, the trends of both show a high degree of consistency. As indicated in Table II, the average time error for reaching the trough values across multiple experimental groups at different heights and speeds is only 3.2%, and the average Fz error is only 2.7%, sufficiently demonstrating the correctness of our proposed model.

V. Conclutions and Future Work

We propose an actuator configuration named RFCA, which can achieve stable operation under conditions of heavy loads, large deformations, and high dynamic impacts. It is a special type of rigid-flexible coupled structure. Unlike typical coupled configurations, where a flexible body is connected to a rigid main body, its flexible element is encapsulated within a rigid shell, forming a nested relationship between the two. This rigid-flexible coupled structure can effectively resist wear and withstand impacts, significantly extending the actuator's service life. However, precisely because of its unique structure, it cannot be accurately solved using conventional rigid-flexible coupled mechanical methods or flexible body mechanics approaches. Particularly challenging is the variation in its equivalent stiffness under large deformation conditions, which directly affects the generality and accuracy of the solution. To address these issues, we propose a rigid-flexible coupled multibody dynamics modeling method suitable for large deformation conditions and obtain the torque–rotation angle curve through static experiments and theoretical derivation. We accurately implement our proposed dynamic model using simulation software. Comparisons between simulation results and multiple sets of dynamic experiments demonstrate the accuracy and effectiveness of our proposed modeling method.

In the future, we will conduct research on integrating the RFCA with mobile robot platforms. We will perform biomimetic observations of sea lions and fish to optimize the design of the RFCA and deploy the optimized RFCA on suitable mobile platforms for amphibious operations. We will apply our proposed modeling method to robot modeling to more accurately compute and predict the state of the robot during motion. Additionally, we will explore expanding the application scope of the RFCA structure to different types of scenarios, achieving better performance in various environments through targeted structural optimization and component selection. Ultimately, we envision extending the RFCA configuration and modeling method to unstructured terrains such as underwater, snow, and sandy environments. This will involve further theoretical and methodological research.

REFERENCES

[1] Y. Yu, J. Liu, Y. You, Q. Tan, X. Xu, Y. Zheng, and Z. Fan, "Modeling and motion analysis of flexible legged robots using the finite particle method," *Thin-Walled Struct.*, vol. 205, pt. B, p. 112491, 2024, doi: 10.1016/j.tws.2024.112491.

[2] S. J. Wang, D. Kuang, S. D. Lee, R. J. Full, and H. S. Stuart, "Squirrel-inspired tendon-driven passive gripper for agile landing," in *Proc. IEEE Int. Conf. Robot. Autom. (ICRA)*, Yokohama, Japan, 2024, pp. 4184–4190, doi: 10.1109/ICRA57147.2024.10610730.

[3] F. Ilievski, A. D. Mazzeo, R. F. Shepherd, X. Chen, and G. M. Whitesides, "Soft robotics for chemists," *Angew. Chem., Int. Ed.*, vol. 50, no. 8, pp. 1890–1895, 2011.

[4] R. Baines, S. K. Patiballa, J. Booth et al. "Multi-environment robotic transitions through adaptive morphogenesis," *Nature*, vol. 610, pp. 283–289, 2022.

[5] T. Chen et al. "Scale-inspired programmable robotic structures with concurrent shape morphing and stiffness variation," Sci. Robot., vol. 9, p. eadl0307, 2024, doi: 10.1126/scirobotics.adl0307.

[6] Y.-J. Kim, H. Song, and C.-Y. Maeng, "BLT gripper: An adaptive gripper with active transition capability between precise pinch and compliant grasp," *IEEE Robot. Autom. Lett.*, vol. 5, no. 4, pp. 5518–5525, Oct. 2020.

[7] M. Yamano et al. "A robot finger with many joints driven by one motor using shape memory gel and tendon-driven mechanism," in *Proc. IEEE Int. Conf. Mechatronics Automat. (ICMA)*, Takamatsu, Japan, Aug. 2021, pp. 1472–1477.

[8] G. Salvietti, Z. Iqbal, M. Malvezzi, T. Eslami, and D. Prattichizzo, "Soft hands with embodied constraints: The soft scoopgripper," in *Proc. IEEE Int. Conf. Robot. Autom. (ICRA)*, Montreal, Canada, May 2019, pp. 2758–2764.

[9] Y. Sun, Q. Zhang, and X. Chen, "Design and analysis of a flexible robotic hand with soft fingers and a changeable palm," *Adv. Robot.*, vol. 34, no. 16, pp. 1041–1054, 2020.

[10] J. H. Low et al. "Sensorized reconfigurable soft robotic gripper system for automated food handling," *IEEE/ASME Trans. Mechatron.*, vol. 27, no. 5, pp. 3232–3243, Oct. 2022.

[11] T. Kim, J. Kim, and S.-C. Yu, "Development of bioinspired multimodal underwater robot 'HERO-BLUE' for Walking, Swimming, and Crawling," *IEEE Trans. Robot.*, vol. 40, pp. 1421–1438, 2024, doi: 10.1109/TRO.2024.3353040.

[12] D. Singhal and V. Narayanamurthy, "Large and small deflection analysis of a cantilever beam," *J. Inst. Eng. India, Ser. A*, vol. 100, no. 1, pp. 83–96, 2019.

[13] M. Pozzi, M. Malvezzi, D. Prattichizzo, and G. Salvietti, "Actuated palms for soft robotic hands: Review and perspectives," *IEEE/ASME Trans. Mechatron.*, vol. 29, no. 2, pp. 902–912, Apr. 2024, doi: 10.1109/TMECH.2023.3328944.

[14] Z. Wang, N. M. Freris, and X. Wei, "SpiRobs: Logarithmic spiral-shaped robots for versatile grasping across scales," *Device*, vol. 3, no. 4, p. 100646, 2025, doi: 10.1016/j.device.2024.100646.

[15] H. J. Kim, S. H. Song, and S. H. Ahn, "A turtle-like swimming robot using a smart soft composite (SSC) structure," *Smart Mater. Structures.*, vol. 22, no. 1, p. 014007, 2012.

[16] A. W. English, "Functional anatomy of the hands of fur seals and sea lions," *Amer. J. Anat.*, vol. 147, no. 1, pp. 1–18, Sep. 1976, doi: 10.1002/aja.1001470102.

[17] X. Ma et al. "Design and optimization of a multimode amphibious robot with propeller-leg," *IEEE Trans. Robot.*, vol. 38, no. 6, pp. 3807–3820, Dec. 2022, doi: 10.1109/TRO.2022.3182880.

[18] S. Zhang, Y. Zhou, M. Xu, X. Liang, J. Liu, and J. Yang, "AmphiHex-I: Locomotory performance in amphibious environments with specially designed transformable flipper legs," *IEEE/ASME Trans. Mechatron.*, vol. 21, no. 3, pp. 1720–1731, Jun. 2016, doi: 10.1109/TMECH.2015.2490074.

[19] M. Verotti, "A pseudo-rigid body model based on finite displacements and strain energy," *Mech. Mach. Theory*, vol. 149, p. 103811, 2020, doi: 10.1016/j.mechmachtheory.2020.103811.